JOURNAL OF GEOPHYSICAL RESEARCH, VOL. 105, NO. A6, PAGES 13,009–13,016, JUNE 1, 2000

Magnetohydrodynamic wave mode conversion in the Earth's magnetotail

J. De Keyser

Belgian Institute for Space Aeronomy, Brussels

Abstract. We study magnetohydrodynamic wave mode conversion as a mechanism contributing to the observed low-frequency electromagnetic fluctuation level in the plasma sheet. Low-frequency waves originating in the magnetosheath can transport energy across the tail flank magnetopause and through the tail lobes toward the plasma sheet. In the plasma sheet boundary layer and in the central plasma sheet, local conditions permit mode conversion to occur in resonant sheets. Resonant coupling to both Alfvén and slow-mode waves is possible. Energy is fed to the plasma in these resonant sheets, which may help to explain the acceleration and heating of particles observed in the plasma sheet boundary layer and the central plasma sheet.

1. Introduction

The magnetotail consists of two lobes with oppositely directed magnetic fields connected to the polar caps, separated by a dense hot central plasma sheet (CPS) where the magnetic field reversal occurs. Much attention has focused on the plasma sheet–lobe interface, also known as the plasma sheet boundary layer (PSBL), as it is believed to be magnetically connected to the auroral regions [e.g., *Cattell et al.*, 1982]. The PSBL is a temporally variable region characterized by counterstreaming particle beams [e.g., *Eastman et al.*, 1984; *Baumjohann et al.*, 1990a; *Parks et al.*, 1998]; an insight in the nature and origin of these beams is of prime importance for understanding auroral processes.

Observations of particle beams in the near-tail PSBL appear to be consistent with an open model of the magnetosphere with a neutral line tailward of the point of observation, where the PSBL would correspond to the separatrix between open and closed magnetic field lines. The persistent presence of the PSBL argues for a continuous operation of field line merging [e.g., *Tsurutani et al.*, 1986; *Takahashi and Hones*, 1988]. The spatial structure and the time variability of high-speed ion beams ("bursty" flows) and their occurrence in both the PSBL and the CPS indicate that additional physical processes must be at work [*Baumjohann et al.*, 1990a; *Parks et al.*, 1998]. Important in this respect are the observations of electrostatic waves in the PSBL [*Baumjohann et al.*, 1990b] and of intense short-duration electric field spikes and low-frequency waves and wave packets in the CPS and the PSBL [*Cattell et al.*, 1982, 1994]. Such electric fields could be responsible for the acceleration and heating of particles and the formation of particle beams [*Hirahara et al.*, 1994]. Stochastic acceleration, for instance, could account for the power law energy spectra typical for plasma sheet particles [e.g., *Zelenyi et al.*, 1990; *Ma and Summers*, 1999].

Several mechanisms may be at the origin of the electric waves found in the PSBL and the CPS. Electrostatic waves have been ascribed to electron beam instabilities [*Omura et al.*, 1996]. Ion multibeam instabilities have been proposed to account for lower frequency waves [*Verheest and Lakhina*, 1991]. In the present paper we examine another mechanism that could contribute to the substantial low-frequency electromagnetic fluctuation level observed in the PSBL: conversion between different magnetohydrodynamic (MHD) wave modes. MHD mode conversion is a process capable of transforming electromagnetic energy carried by waves into kinetic energy. It takes place at plasma and field inhomogeneities where the field-aligned wave vector component matches the local Alfvén or slow-mode wave vectors, thus creating resonant layers where Alfvén or slow-mode waves are excited. In the absence of dissipation the wave amplitudes locally are driven to infinity. If some (anomalous) resistivity is present or if the wave fronts are not exactly planar, the wave amplitude remains bounded. In the first case, energy is dissipated and results in a heating of the plasma in the resonant sheet. In the second case, energy flux in the normal direction is diverted into the tangential directions at the site of resonance. MHD mode conversion has been invoked to address the problem of the heating of the solar corona [e.g., *Poedts et al.*, 1989, and references therein], to explain magnetospheric pulsations [*Southwood*, 1974], and to interpret ULF wave behavior at the Earth's magnetopause [*Belmont et al.*, 1995; *De Keyser et al.*, 1999]. In the present paper we use the techniques introduced by *Belmont et al.* [1995] and extended by *De Keyser et al.* [1999] to examine whether mode conversion could be responsible for the observed electric fields and the acceleration and heating of particles in the CPS and PSBL.

Paper number 2000JA900020.
0148-0227/00/2000JA900020$09.00

We consider the following energy transport scenario: (1) Waves in the magnetosheath (MSH) propagate toward the tail flank magnetopause and boundary layer (MP/BL); these waves may be of solar wind origin, or they might be generated in the magnetosheath, for instance, at the quasi-parallel bow shock. (2) These incident waves can be reflected, transmitted, or resonantly absorbed at the plasma and field inhomogeneity that defines the magnetopause. (3) The wave amplitude in the lobes reaches a finite nonzero level (for propagating waves) or decays exponentially with a characteristic distance of the order of the wavelength (for nonpropagating waves). (4) In both cases the wave amplitude can be significant by the time the wave reaches the PSBL and the CPS. The wave can be transmitted, reflected, or resonantly absorbed at the plasma and field changes in the PSBL and the CPS.

The purpose of this paper is to show that the scenario sketched above can indeed account for energy transport from the magnetosheath to the plasma sheet and plasma sheet boundary layer. We do so by studying mode conversion in the framework of linear nonstatic MHD for wavelengths $1 - 50\ R_E$ and frequencies $5 - 50$ mHz.

2. Geometry and Plasma Properties

We consider a one-dimensional model of the tail, as we are interested in the energy transport in the direction perpendicular to the plasma sheet. The plasma sheet is assumed to be a planar layer parallel to the tail axis; curvature or warping of the plasma sheet, and torsional deformation of the magnetotail [*Tsurutani et al.*, 1986; *Gosling et al.*, 1986] are ignored here. The equilibrium magnetic field is taken to be parallel to this plane; that is, the plasma sheet is a tangential discontinuity. This tail model therefore has no closed field lines. We define x to be perpendicular to the plasma sheet, pointing to the north; z points down the tail; y completes the right-handed frame, pointing duskward. We consider only the northern half of the tail (with typical plasma parameters taken from *Eastman et al.* [1984] and *Tsurutani et al.* [1986]; the temperatures represent the sum of ion and electron temperatures): (1) the central plasma sheet, with equilibrium number density $N_{\rm cps}^{(0)} = 0.3\ {\rm cm}^{-3}$, temperature $T_{\rm cps}^{(0)} = 35 \times 10^6$ K, and tailward bulk flow of $V_{\rm cps}^{(0)} = 200\ {\rm km\ s}^{-1}$; (2) the plasma sheet boundary layer, located at about $D_{\rm cps} = 2\ R_E$ (the plasma sheet thickness is $4\ R_E$); (3) the lobe, with number density $N_{\rm lobe}^{(0)} = 0.02\ {\rm cm}^{-3}$ and temperature $T_{\rm lobe}^{(0)} = 2 \times 10^6$ K; (4) the tail flank magnetopause, located at $x_{\rm mp} = 20\ R_E$ with half-thickness $D_{\rm mp} = 2\ R_E$; and (5) the magnetosheath, with $N_{\rm msh}^{(0)} = 5\ {\rm cm}^{-3}$, $T_{\rm msh}^{(0)} = 2 \times 10^6$ K, and tailward flow of $V_{\rm msh}^{(0)} = 350\ {\rm km\ s}^{-1}$. The lobe magnetic field is $B_{\rm lobe}^{(0)} = 20$ nT. We fix the sense of the 180° magnetic field rotation across the plasma sheet ($B_y^{(0)} > 0$). The magnetosheath magnetic field can have any direction, specified by $\theta_{\rm msh}$, the angle of $\boldsymbol{B}_{\rm msh}^{(0)}$ with the y axis. We adopt an equilibrium number density profile,

$$N^{(0)} = \frac{N_{\rm cps}^{(0)}}{\cosh^2(x/D_{\rm cps})} + N_{\rm lobe}^{(0)}\left(\frac{1}{2}\,{\rm erfc}\,\frac{x - x_{\rm mp}}{D_{\rm mp}} - \frac{1}{\cosh^2(x/D_{\rm cps})}\right) + \frac{N_{\rm msh}^{(0)}}{2}\,{\rm erfc}\left(-\frac{x - x_{\rm mp}}{D_{\rm mp}}\right),$$

with the corresponding temperature and tailward velocity profiles. The magnetic field angle in the y-z plane is defined by

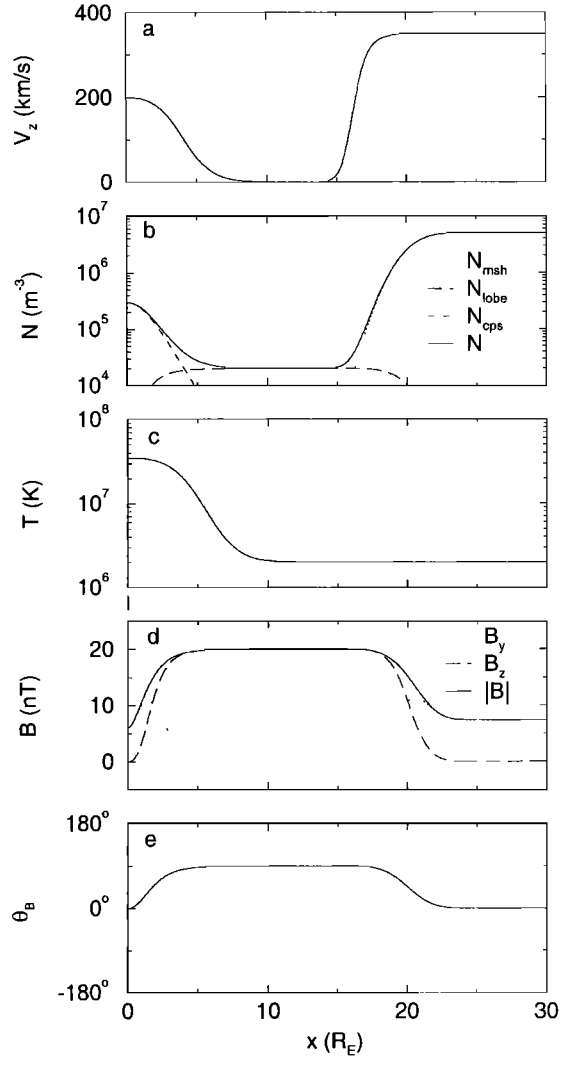

Figure 1. Equilibrium state of the magnetotail adopted in the simulations, for a magnetosheath field direction $\theta_{\rm msh} = 0°$. The plasma sheet and the magnetopause/boundary layer both have a characteristic half-width of $2\ R_E$. Only the northern half of the plasma sheet–lobe–magnetosheath system is shown. (a) Tailward velocity. (b) Magnetosheath, lobe, plasma sheet, and total number density. (c) Temperature. (d) Magnetic field components parallel to the plasma sheet and field strength. (e) Magnetic field orientation (0° is dawn-to-dusk, 90° is tailward); the magnetic field rotation across the plasma sheet is 180° (of which only the northern half is plotted).

$$\theta = 90°\left(\frac{1}{2}\,\mathrm{erfc}\,\frac{x-x_{\mathrm{mp}}}{D_{\mathrm{mp}}} - \frac{1}{\cosh^2(x/D_{\mathrm{cps}})}\right) + \frac{\theta_{\mathrm{msh}}}{2}\,\mathrm{erfc}\left(-\frac{x-x_{\mathrm{mp}}}{D_{\mathrm{mp}}}\right).$$

The equilibrium structure is then completely determined by pressure balance, and is illustrated in Figure 1.

One of the conditions for MHD theory to be valid is that the length scales involved exceed the gyroradius scales. The ion gyroradius (for the values adopted above, and supposing that the total temperature is due to protons only) is 0.041 R_E in the magnetosheath, 0.015 R_E in the lobe, and 0.21 R_E at the center of the plasma sheet (this value strongly depends on the magnetic field minimum in the neutral sheet). We therefore only consider tangential wavelengths $\lambda_t > 1\ R_E$. MHD resonant layers are (in the absence of dissipation) infinitely thin; the usefulness of the MHD description near the resonance is therefore limited. The one-dimensional approximation is reasonable only for wavelengths $\lambda_t < 50\ R_E$, smaller than the tail diameter.

The proton gyrofrequency is 110 mHz in the magnetosheath, 300 mHz in the lobe, and 90 mHz at the center of the plasma sheet, placing an upper limit on the frequencies in the MHD model. In the tail lobes the Alfvén and slow-mode wave travel times from the midtail to the ionosphere are of the order of hundreds of seconds (even longer in the MP/BL, the CPS, and the PSBL); the behavior of resonant waves with longer periods (lower frequencies) is affected by the ionospheric response. Field-aligned particle traveling times (especially for the electrons) from the midtail to the ionosphere set a similar lower limit on the frequencies for which the MHD simulations retain their local character. We therefore consider only frequencies between 5 and 50 mHz.

3. Linear Perturbation Analysis

We linearize the ideal MHD equations around the equilibrium configuration described in the previous section, by writing every quantity (depending on the position vector $\boldsymbol{r}$ and time t) as a sum of a one-dimensional equilibrium value and higher-order contributions: $q(\boldsymbol{r},t) = q^{(0)}(x) + q^{(1)}(\boldsymbol{r},t) + \ldots$. In particular, we consider monochromatic waves with circular frequency $\omega = 2\pi f$ and wave vectors $\boldsymbol{k} = k_x(x)\mathbf{1}_x + \boldsymbol{k}_t$, where $\boldsymbol{k}_t = [0, k_y, k_z]$ is a constant tangential wave vector, of the form

$$q^{(1)}(\boldsymbol{r},t) = \hat{q}(x)\mathrm{e}^{i(\boldsymbol{k}_t\boldsymbol{r}-\omega t)}.$$

The linearized MHD equations can then be expressed in terms of the normal displacement $\hat{\xi}_x$ and the total pressure perturbation $\hat{\tau}$ as

$$\frac{d}{dx}\hat{\tau} = C_1(x,\boldsymbol{k}_t,\omega)\hat{\xi}_x,$$
$$\frac{d}{dx}\hat{\xi}_x = C_2(x,\boldsymbol{k}_t,\omega)\hat{\tau}.$$

Expressions for C_1 and C_2, as well as for all other perturbations in terms of $\hat{\xi}_x$ and $\hat{\tau}$, are given in the appendix. Defining $K_x^2 = -C_1C_2$, we find that these equations reduce in uniform regions to

$$\left(\frac{d^2}{dx^2} + K_x^2\right)\hat{\xi}_x = 0.$$

As ω is real, and as $\boldsymbol{k}_t$ is real for plane waves, K_x^2 is real as well. If $K_x^2 > 0$, the solution is a superposition of a left and a right going sinusoidal wave, with $k_x = \pm K_x$ (propagating waves). If $K_x^2 < 0$, the solution is a superposition of an exponentially growing and decaying mode, with $k_x = \pm i\sqrt{-K_x^2}$ (nonpropagating waves). When C_2 becomes unbounded at some point in the domain (C_1 is always bounded), K_x^2 is unbounded there (when $C_1 \neq 0$) and the corresponding spatial scale tends to zero.

Belmont et al. [1995] and *De Keyser et al.* [1999] have presented a detailed analysis for the static MHD case (equilibrium flow $\boldsymbol{v}^{(0)}=\boldsymbol{0}$) of the conditions for which wave propagation is possible, as well as of the conditions for which singularities occur. In the appendix it is shown that the same analysis holds for nonstatic MHD if one replaces ω by the Doppler-shifted frequency $\tilde{\omega} = \omega - \boldsymbol{k}_t\cdot\boldsymbol{v}^{(0)}$, so we do not repeat it here. The conditions for singularities to occur are precisely the dispersion relations for Alfvén and slow-mode waves: A resonant coupling between the fast magnetosonic waves propagating in the x direction and the tangential Alfvén and slow-mode waves exists at these singular points. The resonance conditions are

$$|k_\parallel| = k_A = \frac{\tilde{\omega}}{v_A},$$
$$|k_\parallel| = k_S = \frac{\tilde{\omega}}{v_A}\sqrt{v_A^2 + c_s^2},$$

where c_s is the speed of sound and v_A is the Alfvén velocity; k_A and k_S are the local Alfvén and slow-mode wave vectors.

The singularities of the ideal MHD solutions at resonant points can be removed by introducing a dissipation term. Another way to deal with these singularities, proposed by *Belmont et al.* [1995], is by considering surface wave vectors $\boldsymbol{k}_t + \epsilon_t i$ that have a small imaginary part ($\epsilon_t/k_t \ll 1$). The wave fronts then are modulated in the tangential direction with a length scale $\sim \epsilon_t^{-1} \gg \lambda_t$, rather than being exactly planar. Introducing such an imaginary part avoids the zeros in the denominator of C_2, and the singularities disappear. Since ω is real, Im $K_x^2 \neq 0$ in general: The amplitudes of waves propagating through a uniform medium no longer remain constant, and the time-averaged energy flux $\langle\phi_x\rangle$ changes with x at a rate proportional to ϵ_t. It is therefore important to choose ϵ_t sufficiently small so as to approximate the equations for the plane wave case. It can be shown, for suitably small ϵ_t, that the magnitude of the jump in the energy flux at the resonant points does not depend on the precise value of ϵ_t (see the appendix); the sign of the jump, however, depends on the direction of ϵ_t with respect to the magnetic field and the flow velocity. In the static case, *Belmont et al.* [1995] chose ϵ_t so that $\boldsymbol{k}_t\cdot\epsilon_t = 0$: Then Im $K_x^2 = 0$, and $\langle\phi_x\rangle$ remains exactly constant except at

the resonances. In the nonstatic case, no single choice of ϵ_t can make K_x^2 real everywhere. In our simulations we have chosen ϵ_t either manually, or by requiring that K_x^2 would be real in the magnetosheath by numerically finding the zero of Im K_x^2 as a function of ϵ_y (when ϵ_z is given) or of ϵ_z (when ϵ_y is given).

We impose boundary conditions at the center of the plasma sheet. As the wave solutions are determined up to a scaling factor, we set $\hat{\xi}_x(0) = 1$. We require that only a left going wave is present at this boundary, that is, that the phase difference between $\hat{\xi}_x$ and $\hat{\tau}$ remains constant:

$$\frac{d}{dx}\frac{\hat{\tau}}{\hat{\xi}_x} = \left(\hat{\tau}\frac{d\hat{\xi}_x}{dx} - \hat{\xi}_x\frac{d\hat{\tau}}{dx}\right)/\hat{\xi}_x^2 = 0.$$

This amounts to requiring that

$$(\hat{\tau}/\hat{\xi}_x)^2 = C_1/C_2.$$

Hence, $\hat{\tau}(0) = \pm\hat{\xi}_x(0)\sqrt{C_1(0)/C_2(0)}$, where the sign has to be chosen so as to select the left going wave.

We solve the pair of linear first-order ordinary differential equations for $\hat{\xi}_x$ and $\hat{\tau}$ using an adaptive second-order accurate implicit complex integration scheme. We have chosen $\epsilon_t/k_t \sim 10^{-8}$, small enough to obtain a good approximation to the plane wave case. Thanks to the adaptivity of the integrator we are able to resolve the resonant sheet, whose thickness scales with ϵ_t. We have verified the independence of the $\langle\phi_x\rangle$ profile on the value of ϵ_t.

4. Wave Solutions

We first consider monochromatic waves with a frequency $f = 10$ mHz and wave vectors $\boldsymbol{k}_t \parallel \mathbf{1}_z$ and focus on the effects of the magnitude of the tangential wave vector and the direction of the magnetosheath magnetic field.

The magnetosheath Alfvén velocity is 72 km s^{-1}, which corresponds to a tangential wavelength $\lambda_{A,\mathrm{msh}} = 1.13\ R_E$. In the cold plasma case all waves with a larger wavelength are propagating; in the warm plasma case the propagation domain is more complicated as the minimum wavelength for propagation depends on the direction of $\boldsymbol{k}_t$, but $\lambda_t \gtrsim \lambda_{A,\mathrm{msh}}$ remains an approximate propagation condition [see *De Keyser et al.*, 1999]. In addition, this limit roughly coincides with the lower wavelength limit for the MHD approximation set by the ion gyroradius scales.

As a first example we consider a dawn to dusk interplanetary magnetic field, that is, $\theta_{\mathrm{msh}} = 0°$: The magnetic field rotates over 90° across the northern tail flank magnetopause. Figure 2a shows the wave solution for a wavelength $\lambda_t = 12\ R_E$. The imaginary part of the wave vector was chosen as $\epsilon_t = (0, -10^{-8}k_t)$. The plots show the maximum modulus of the magnetic field fluctuations $\boldsymbol{B}^{(1)}$ (in arbitrary units), the time-averaged energy flux $\langle\phi_x\rangle$ normalized to the energy flux carried by the incident magnetosheath wave, and the wave vector diagram with the field aligned component of the tangential wave vector $k_\parallel$ as well as the k_A and k_S profiles, which allows us to identify the nature of the resonances. From the amplitude of the magnetic field fluctuations we see that the incident waves are indeed propagating through the magnetosheath, but not in the lobe as the fluctuation amplitude rapidly decays to zero: The incident waves penetrate into the lobe up to a distance of the order of the normal wavelength but are reflected. At the same time, however, we observe a sharp peak in the MP/BL: An Alfvén resonance occurs at the point where $k_\parallel = k_A(x)$; the fluctuation level becomes very high in a narrow layer. This is reflected in the energy flux profile: While the flux remains constant in the magnetosheath and in the lobe, there is a pronounced discontinuous jump at the site of resonance, whose magnitude corresponds to the energy flux that is diverted there into the tangential directions. The wave vector diagram shows that there is an Alfvén resonance in the PSBL as well; the associated energy flux jump, however, is very small. While 7% of the incident energy flux is diverted at the MP/BL resonance, only 0.00005% is diverted at the PSBL resonance. This is essentially due to the fact that the lobe is not transparent for the incident waves. One can also infer from the wave vector diagram that two additional slow-mode resonances will occur in the PSBL for smaller wavelengths; the energy flux reaching these resonances, however, is extremely small.

Waves with a larger wavelength can more easily penetrate into the lobes. Figure 2b shows the solution for $\lambda_t = 24\ R_E$, $\theta_{\mathrm{msh}} = 0°$, with the same ϵ_t as before. Although the wave is still nonpropagating in the lobes, its penetration depth is larger. The figure shows the two Alfvén resonances, each of which is responsible for diverting 0.04% of the incident wave energy. Note that the flux reaching the center of the plasma sheet (where the boundary condition requires that only left going waves are present) no longer is zero. In Figure 2c we consider the same wavelength; now there is no magnetic field rotation across the northern tail flank magnetopause ($\theta_{\mathrm{msh}} = 90°$). In the particular $\boldsymbol{k}_t \parallel \boldsymbol{B}^{(0)}$ configuration in the MP/BL region, no energy flux is diverted into the tangential directions at the MP/BL Alfvén resonance; the flux diverted at the PSBL resonance remains about 0.04% of the incident wave energy. For a dusk to dawn magnetosheath field ($\theta_{\mathrm{msh}} = 180°$) we obtain an energy flux identical to that of Figure 2b. This can be seen from the symmetry of the equations when $\boldsymbol{k}_t \parallel \mathbf{1}_z$; the only change in the solution is the reversed sign of $B_y^{(1)}$ and $v_y^{(1)}$, that is, the polarization sense of the waves is reversed.

The sign of the energy flux jumps depends on the orientation of the imaginary part of the wave vector. This is shown for the case $\theta_{\mathrm{msh}} = 180°$, $\epsilon_t = (-10^{-8}k_t, 0)$, in Figure 2d: While energy from the tangential waves is diverted into the normal direction at the MP/BL resonance, the opposite process occurs at the PSBL resonance. This illustrates that the technique of considering nonplanar waves is more general than the introduction of a dissipation mechanism, which is irreversible and can only lead to absorption of energy.

The previous examples show how the energy that reaches the PSBL resonance increases as the wavelength becomes larger. For larger wavelengths, however, no resonances occur any more, unless we reduce the frequency. Figure 2e shows the case $f = 5$ mHz, $\lambda_t = 48\ R_E$, $\theta_{\mathrm{msh}} = 0°$. About

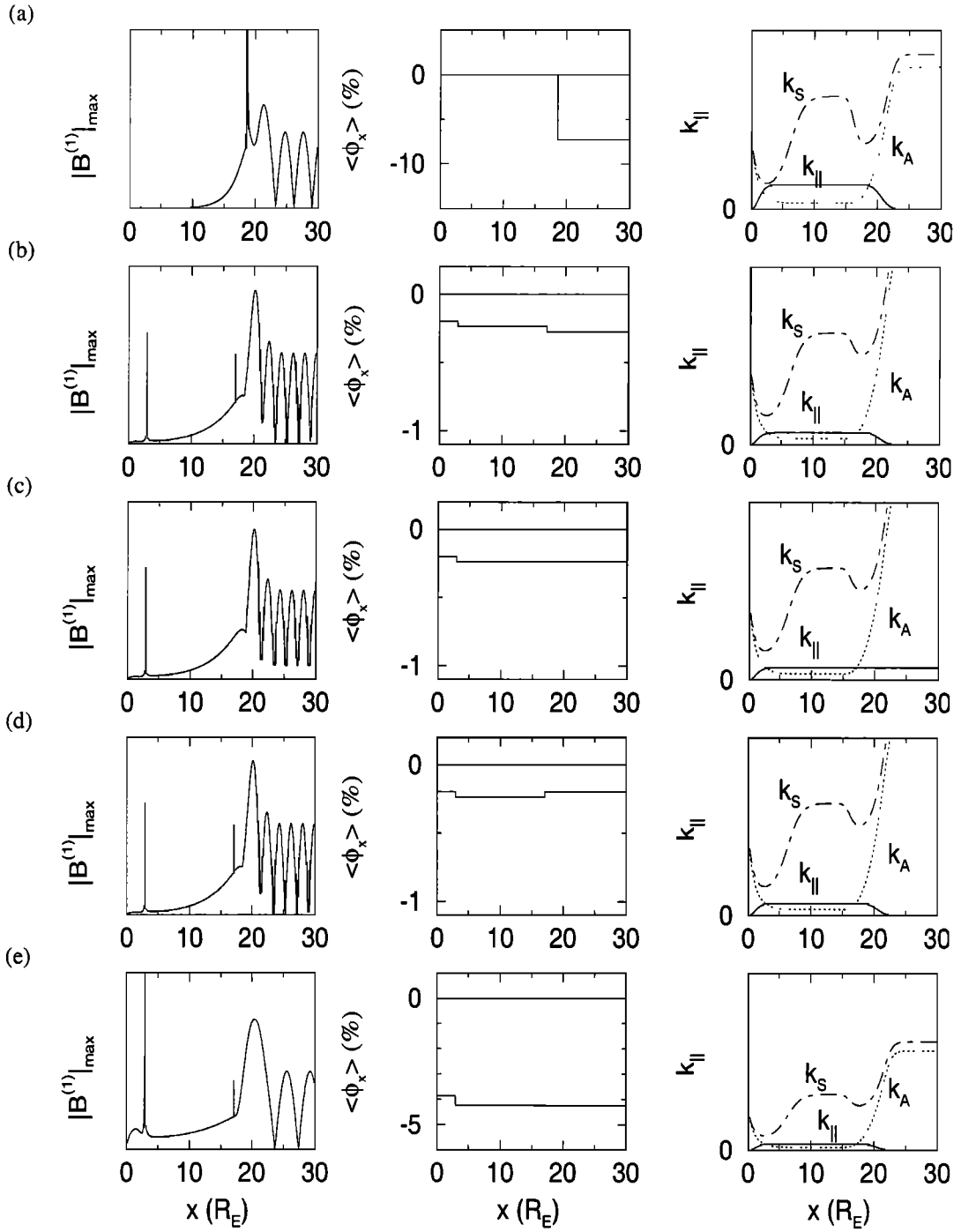

Figure 2. Wave solutions for different frequency-wavelength combinations and various orientations of the magnetosheath magnetic field. Left plots show wave amplitude (maximum value of $|\boldsymbol{B}^{(1)}|$) in arbitrary units (the solution is determined only up to a scaling factor). Middle plots show energy flux $\langle\phi_x\rangle$ normalized to the energy flux carried by the incident magnetosheath waves. Right plots show wave vector diagram with the profiles of $k_{||}$ and the Alfvén and slow-mode wave vectors k_A, and k_S; the intersections of $k_{||}$ with k_A and k_S correspond to the resonances. Parameters and orientations are (a) $f = 10$ mHz, $\lambda_t = 12\ R_E$, $\theta_{\rm msh} = 0°$: significant resonance only at the MP/BL; (b) $f = 10$ mHz, $\lambda_t = 24\ R_E$, $\theta_{\rm msh} = 0°$ or 180°: resonances at the MP/BL and in the PSBL; (c) $f = 10$ mHz, $\lambda_t = 24\ R_E$, $\theta_{\rm msh} = 90°$: significant resonance only in the PSBL; (d) $f = 10$ mHz, $\lambda_t = 24\ R_E$, $\theta_{\rm msh} = 180°$, with a different orientation of the imaginary part of the wave vector: Energy is fed to the system at the MP/BL resonance, while energy is removed from the system at the PSBL resonance; and (e) $f = 5$ mHz, $\lambda_t = 48\ R_E$, $\theta_{\rm msh} = 0°$: resonance at the PSBL with an energy flux jump of 0.4% of the incident magnetosheath flux.

0.4% of the incident wave energy is converted into tangential waves at the resonance.

5. Discussion

The purpose of this paper was to evaluate a scenario for the deposit of energy in spatially localized layers in the plasma sheet and plasma sheet boundary layer. We have developed a nonstatic linear MHD model to examine the propagation of electromagnetic waves for wavelengths ranging from 1 to 50 R_E and for frequencies from 5 to 50 mHz. We have found that such MHD waves can indeed transport electromagnetic energy from the shocked solar wind in the magnetosheath across the tail flank magnetopause and through the lobe to the plasma sheet and the plasma sheet boundary layer, where mode conversion excites Alfvén or slow-mode waves in thin resonant sheets. The associated fluctuating electric fields could play a role in the acceleration of plasma sheet particles.

A more complete picture of the energy transport from the magnetosheath to the PSBL should be obtained in the future by considering, for each frequency of the incident wave spectrum, a superposition of the different wave vectors compatible with the dispersion equation. This is the proper way to introduce the external origin of the waves, including, for instance, the coupling to the ionosphere, and therefore to determine the overall changes of the normal energy flux at the resonances.

The presence of magnetosheath waves is a prerequisite in the proposed model. Solar wind pressure variations are known to have a very broad frequency content that overlaps with the range of interest here, and can act as the external driver of the oscillations in our model. Alternatively, such waves could be generated in the magnetosheath, as, for instance, turbulence originating at the quasi-parallel bow shock. The calculations presented here show that only a small fraction of the incident wave energy, generally of the order of 0.1%, can be delivered to the plasma sheet, as most of the waves are reflected since the lobe is not transparent for the magnetosheath waves. However, because of the high magnetosheath fluctuation level and the relatively low plasma sheet density, the energy flux per particle can be important. Another possible source that could drive waves into the lobes is the Kelvin-Helmholtz instability at the magnetopause, which is characterized by frequencies ranging from several to 100 mHz and by wavelengths of several Earth radii [e.g., *Walker*, 1981], that is, within the frequency and wavelength ranges that were studied here. In that case, however, the waves are nonpropagating in the magnetosheath; the driver is internal rather than external, a situation that was not considered here. Energy can then leak from the oscillating magnetospheric boundary layer and can be fed to plasma sheet resonances in a way similar to that described here.

The analysis presented here has several limitations. We have simplified the problem geometry, and we have ignored the coupling of the tail with the near-Earth environment and the ionosphere. We have only studied monochromatic waves; in reality, pulses and wave packets are often present. Limitations also arise from the neglect of kinetic effects (ion gyroradius length scale, ion gyration frequency). Electron inertia effects are unimportant due to the low-frequencies considered here. When the wave's phase velocity is of the same order as the thermal velocity, as in the warm plasma sheet, an MHD approximation with an adiabatic closure relation might no longer be appropriate. In spite of these limitations, mode conversion appears to be a plausible mechanism contributing to the substantial low-frequency electromagnetic fluctuation level observed in the plasma sheet and the plasma sheet boundary layer; the magnitude of this contribution remains to be assessed from observations.

Appendix: Linearized MHD Equations

This appendix describes the linearization of the nonstatic ideal MHD equations [see also *Walker*, 1981; *De Keyser et al.*, 1999]. Let x be the normal to the plasma sheet. We denote the mass density by ρ, the bulk velocity by $\boldsymbol{v}$, and the magnetic and electric fields by $\boldsymbol{B}$ and $\boldsymbol{E}$. The thermal pressure is $p = k_B \rho T/m$, where k_B is Boltzmann's constant, m the (ion + electron) mass, and T the (ion + electron) temperature. The specific energy is $\mathcal{E} = \rho v^2/2 + B^2/2\mu_0 + p/(\gamma - 1)$, where $\gamma = \frac{5}{3}$ is the ratio of specific heats. Conservation of mass, momentum, and energy are expressed by

$$\frac{\partial \rho}{\partial t} + \nabla\cdot(\rho \boldsymbol{v}) = 0, \quad \text{(A1)}$$

$$\frac{\partial \rho \boldsymbol{v}}{\partial t} + \nabla\cdot[\rho \boldsymbol{v}\boldsymbol{v} + (p + \frac{B^2}{2\mu_0})\boldsymbol{I} - \frac{1}{\mu_0}\boldsymbol{B}\boldsymbol{B}] = \boldsymbol{0}, \quad \text{(A2)}$$

$$\frac{\partial \mathcal{E}}{\partial t} + \nabla\cdot[(\frac{\rho v^2}{2} + \frac{\gamma p}{\gamma - 1})\boldsymbol{v} + \frac{1}{\mu_0}\boldsymbol{E}\times\boldsymbol{B}] = 0. \quad \text{(A3)}$$

Ideal MHD includes only the convection electric field, and Maxwell's equations become

$$\boldsymbol{E} + \boldsymbol{v}\times\boldsymbol{B} = \boldsymbol{0}, \quad \text{(A4)}$$

$$\frac{\partial \boldsymbol{B}}{\partial t} + \nabla\times\boldsymbol{E} = \boldsymbol{0}, \quad \text{(A5)}$$

$$\nabla\cdot\boldsymbol{B} = 0. \quad \text{(A6)}$$

Let $\boldsymbol{\xi}(\boldsymbol{r}, t)$ denote the current position of a plasma element that was at position $\boldsymbol{r}$ at a reference time t_0; then

$$\boldsymbol{v} = \frac{d\boldsymbol{\xi}}{dt} = \frac{\partial \boldsymbol{\xi}}{\partial t} + (\boldsymbol{v}\cdot\nabla)\boldsymbol{\xi}. \quad \text{(A7)}$$

We further define the isotropic total pressure by

$$\tau = p + \frac{B^2}{2\mu_0}. \quad \text{(A8)}$$

We write all quantities in the form $q(\boldsymbol{r}, t) = q^{(0)}(x) + q^{(1)}(\boldsymbol{r}, t) + q^{(2)}(\boldsymbol{r}, t) + \ldots$, where $q^{(0)}$ is the one-dimensional equilibrium state, and $q^{(1)}$ and $q^{(2)}$ are the first- and second-order perturbations. We consider monochromatic waves with circular frequency $\omega = 2\pi f$ and tangential wave vector $\boldsymbol{k}_t = [0, k_y, k_z]$ of the form $q^{(1)} = \hat{q}(x)e^{i(\boldsymbol{k}_t\boldsymbol{r} - \omega t)}$. The second-order perturbations then consist of waves with frequencies $\omega \pm \omega$: a dc and a double frequency component. We will denote the average of $q^{(2)}$ over y, z, and t (that is,

the dc component) by $\langle q^{(2)}\rangle = \hat{q}\,(x)$. The spatial derivatives are given by the operator $\boldsymbol{\nabla} \equiv [d/dx, 0, 0]$ for equilibrium quantities, and by $\hat{\boldsymbol{\nabla}} \equiv [d/dx, ik_y, ik_z]$ for first-order perturbations. The time derivatives are $d/dt \equiv 0$ for zero-order, and $d/dt \equiv (-i\omega)$ for first-order quantities.

For the one-dimensional case, the zero-order equations reduce to $d\tau^{(0)}/dx = 0$, that is, the pressure balance condition.

Introducing the Doppler-shifted frequency $\tilde{\omega} = \omega - \omega_0$ with $\omega_0 = \boldsymbol{k}_t \boldsymbol{v}^{(0)}$, and defining $\kappa_0 = \boldsymbol{k}_t \boldsymbol{B}^{(0)}$, the first-order equations can be written as

$$
\begin{aligned}
-i\tilde{\omega}\hat{\rho} + (\hat{\boldsymbol{\nabla}}\cdot\hat{\boldsymbol{v}} + \hat{\boldsymbol{v}}\cdot\boldsymbol{\nabla})\rho^{(0)} &= 0,\\
-i\tilde{\omega}\rho^{(0)}\hat{\boldsymbol{v}} + \hat{\boldsymbol{\nabla}}\hat{\tau} - [(\hat{\boldsymbol{B}}\cdot\boldsymbol{\nabla})\boldsymbol{B}^{(0)} + i\kappa_0\hat{\boldsymbol{B}}]/\mu_0 & \\
+\rho^{(0)}(\hat{\boldsymbol{v}}\cdot\boldsymbol{\nabla})\boldsymbol{v}^{(0)} &= \boldsymbol{0},\\
-i\tilde{\omega}(\hat{p} - c_s^2\hat{\rho}) + \hat{\boldsymbol{v}}\cdot\boldsymbol{\nabla}p^{(0)} - c_s^2\hat{\boldsymbol{v}}\cdot\boldsymbol{\nabla}\rho^{(0)} &= 0,\\
\hat{\boldsymbol{E}} + \hat{\boldsymbol{v}}\times\boldsymbol{B}^{(0)} + \boldsymbol{v}^{(0)}\times\hat{\boldsymbol{B}} &= \boldsymbol{0},\\
-i\tilde{\omega}\hat{\boldsymbol{B}} - i\kappa_0\hat{\boldsymbol{v}} + (\hat{\boldsymbol{\nabla}}\cdot\hat{\boldsymbol{v}} + \hat{\boldsymbol{v}}\cdot\boldsymbol{\nabla})\boldsymbol{B}^{(0)} &= \boldsymbol{0},\\
\hat{\boldsymbol{\nabla}}\cdot\hat{\boldsymbol{B}} &= 0,\\
i\tilde{\omega}\hat{\boldsymbol{\xi}} + \hat{\boldsymbol{v}} &= \boldsymbol{0},\\
-\hat{\tau} + \hat{p} + \boldsymbol{B}^{(0)}\cdot\hat{\boldsymbol{B}}/\mu_0 &= 0,
\end{aligned}
$$

where $c_s^2 = \gamma p^{(0)}/\rho^{(0)}$ defines the local speed of sound. All perturbed quantities can be expressed in terms of $\hat{\xi}_x$ and $\hat{\tau}$, which are found by solving the pair of ordinary differential equations

$$\frac{d}{dx}\hat{\tau} = C_1\hat{\xi}_x = \rho^{(0)}\Omega_{kA}^2\hat{\xi}_x, \tag{A9}$$

$$\frac{d}{dx}\hat{\xi}_x = C_2\hat{\tau} = -\left(\frac{\tilde{\omega}^2}{v_A^2 + c_s^2\Omega_{kA}^2/\tilde{\omega}^2} - k_t^2\right)\frac{\hat{\tau}}{\rho^{(0)}\Omega_{kA}^2}, \tag{A10}$$

where $\Omega_{kA}^2 = \tilde{\omega}^2 - \omega_{kA}^2$ and $\omega_{kA} = \boldsymbol{k}_t\boldsymbol{v}_A$, with the Alfvén velocity $\boldsymbol{v}_A = \boldsymbol{B}^{(0)}/\sqrt{\mu_0\rho^{(0)}}$. These equations are identical to those for the static case [see *De Keyser et al.*, 1999] in which ω is replaced by $\tilde{\omega}$. The other linear perturbations are then found as

$$\hat{\rho} = -\frac{d\rho^{(0)}}{dx}\hat{\xi}_x + \frac{\hat{\tau}}{v_A^2 + c_s^2\Omega_{kA}^2/\tilde{\omega}^2},$$

$$\hat{p} = -\frac{dp^{(0)}}{dx}\hat{\xi}_x + \frac{c_s^2\hat{\tau}}{v_A^2 + c_s^2\Omega_{kA}^2/\tilde{\omega}^2},$$

$$\hat{v}_x = -i\tilde{\omega}\hat{\xi}_x,$$

$$\hat{v}_y = -\frac{dv_y^{(0)}}{dx}\hat{\xi}_x + \frac{\tilde{\omega}\hat{\tau}}{\rho^{(0)}\Omega_{kA}^2}\left(k_y - \frac{\omega_{kA}v_{Ay}}{v_A^2 + c_s^2\Omega_{kA}^2/\tilde{\omega}^2}\right),$$

$$\hat{v}_z = -\frac{dv_z^{(0)}}{dx}\hat{\xi}_x + \frac{\tilde{\omega}\hat{\tau}}{\rho^{(0)}\Omega_{kA}^2}\left(k_z - \frac{\omega_{kA}v_{Az}}{v_A^2 + c_s^2\Omega_{kA}^2/\tilde{\omega}^2}\right),$$

$$\hat{B}_x = i\kappa_0\hat{\xi}_x,$$

$$\hat{B}_y = -\frac{dB_y^{(0)}}{dx}\hat{\xi}_x + \frac{\hat{\tau}}{\rho^{(0)}\Omega_{kA}^2}\left(-\kappa_0 k_y + \frac{\tilde{\omega}^2 B_y^{(0)}}{v_A^2 + c_s^2\Omega_{kA}^2/\tilde{\omega}^2}\right),$$

$$\hat{B}_z = -\frac{dB_z^{(0)}}{dx}\hat{\xi}_x + \frac{\hat{\tau}}{\rho^{(0)}\Omega_{kA}^2}\left(-\kappa_0 k_z + \frac{\tilde{\omega}^2 B_z^{(0)}}{v_A^2 + c_s^2\Omega_{kA}^2/\tilde{\omega}^2}\right).$$

We use the time-averaged second-order equations to determine $\langle v_x^{(2)}\rangle$ and $\langle B_x^{(2)}\rangle$. From the second-order expansion of (A7), and from (A5) and (A4) we find, respectively

$$\hat{v}_x = \frac{1}{2}\mathrm{Re}\{(\hat{\boldsymbol{v}}^*\cdot\hat{\boldsymbol{\nabla}})\hat{\xi}_x\}, \tag{A11}$$

$$\boldsymbol{v}^{(0)}\hat{B}_x - \boldsymbol{B}^{(0)}\hat{v}_x = \frac{1}{2}\mathrm{Re}\{\hat{\boldsymbol{B}}\hat{v}_x^* - \hat{\boldsymbol{v}}\hat{B}_x^*\}, \tag{A12}$$

where an asterisk denotes complex conjugation.

The mass flux vector is $\boldsymbol{\psi} = \rho\boldsymbol{v}$. The time-averaged mass flux across the one-dimensional structure is found, using (A11), as

$$\begin{aligned}\langle\psi_x\rangle &= \langle\psi_x^{(2)}\rangle = \langle\rho^{(1)}\boldsymbol{v}^{(1)} + \rho^{(0)}\boldsymbol{v}^{(2)}\rangle\\ &= \frac{1}{2}\mathrm{Re}\{\hat{\rho}\hat{\boldsymbol{v}}^*\} + \rho^{(0)}\hat{v}_x = \frac{\tilde{\omega}}{2}\frac{d\rho^{(0)}}{dx}\mathrm{Im}\{\xi\xi^*\} = 0.\end{aligned}$$

The energy flux is

$$\boldsymbol{\phi} = \left(\frac{\rho v^2}{2} + \frac{\gamma p}{\gamma - 1}\right)\boldsymbol{v} + \frac{1}{\mu_0}\boldsymbol{E}\times\boldsymbol{B},$$

where the first term represents the kinetic energy flux and the second term the electromagnetic Poynting flux. The time-averaged energy flux can be computed using (A11) and (A12):

$$\begin{aligned}\langle\phi_x\rangle &= \langle\phi_x^{(2)}\rangle\\ &= \langle v_x^{(1)}\left(\frac{1}{2}\rho^{(1)}v^{(0)2} + \rho^{(0)}\boldsymbol{v}^{(0)}\cdot\boldsymbol{v}^{(1)} + \frac{\gamma}{\gamma - 1}p^{(1)}\right)\rangle\\ &\quad + \left(\frac{1}{2}\rho^{(0)}v^{(0)2} + \frac{\gamma}{\gamma - 1}p^{(0)}\right)\langle v_x^{(2)}\rangle\\ &\quad + \frac{1}{\mu_0}[(\boldsymbol{E}^{(0)}\times\langle\boldsymbol{B}^{(2)}\rangle)_x + (\langle\boldsymbol{E}^{(1)}\times\boldsymbol{B}^{(1)}\rangle)_x\\ &\qquad + (\langle\boldsymbol{E}^{(2)}\rangle\times\boldsymbol{B}^{(0)})_x].\end{aligned}$$

After some algebra, we find that

$$\langle\phi_x\rangle = \frac{\omega}{2}\mathrm{Im}\{\hat{\xi}_x\hat{\tau}^*\},$$

that is, the normal energy flux is the normal displacement times the total normal pressure. The change in energy flux over an interval $[a, b]$ is

$$\Delta\langle\phi_x\rangle = \int_a^b \frac{d\langle\phi_x\rangle}{dx}dx = \frac{\omega}{2}\int_a^b \mathrm{Im}\{C_1^*\hat{\xi}_x\hat{\xi}_x^* + C_2\hat{\tau}\hat{\tau}^*\}dx.$$

Using Cauchy's theorem at the singular points, we find

$$\Delta\langle\phi_x\rangle = \frac{\omega\pi}{2}\sum_{x_\alpha} \pm \lim_{x\to x_\alpha}(x - x_\alpha)[C_1^*\hat{\xi}_x\hat{\xi}_x^* + C_2\hat{\tau}\hat{\tau}^*],$$

where the sum extends over all singular points x_α in the interval. In the absence of singularities, $\langle\phi_x\rangle$ remains constant. Otherwise, the energy flux changes discontinuously at each x_α. The sign of each jump depends on how the integration path in the complex plane is chosen when applying the Cauchy theorem.

Acknowledgments. The author wants to thank Michel Roth and Vladimir Cadez for valuable discussions. This work was supported by PRODEX contracts with ESA in the framework of the Ulysses and Cluster II projects. The support of the Belgian Federal Office for Scientific, Technical and Cultural Affairs is acknowledged.

Michel Blanc thanks Gérard Belmont and A. David M. Walker for their assistance in evaluating this paper.

References

Baumjohann, W., G. Paschmann, and H. Lühr, Characteristics of high-speed ion flows in the plasma sheet, *J. Geophys Res., 95*, 3801–3809, 1990a.

Baumjohann, W., R. A. Treumann, and J. LaBelle, Average electric wave spectra in the plasma sheet: Dependence on ion density and ion beta, *J. Geophys. Res., 95*, 3811–3817, 1990b.

Belmont, G., F. Reberac, and L. Rezeau, Resonant amplification of magnetosheath MHD fluctuations at the magnetopause, *Geophys. Res Lett., 22*, 295–298, 1995.

Cattell, C. A., M. Kim, R. P. Lin, and F. S Mozer, Observations of large electric fields near the plasmasheet boundary by ISEE-1, *Geophys. Res. Lett., 9*, 539–542, 1982.

Cattell, C., F. Mozer, K. Tsuruda, H. Hayakawa, M. Nakamura, T. Okada, S Kokubun, and T. Yamamoto, Geotail observations of spiky electric fields and low-frequency waves in the plasma sheet and plasma sheet boundary, *Geophys. Res. Lett., 21*, 2987–2990, 1994.

De Keyser, J., M. Roth, F. Reberac, L. Rezeau, and G. Belmont, Resonant amplification of MHD waves in realistic subsolar magnetopause configurations, *J. Geophys. Res., 104*, 2399–2409, 1999.

Eastman, T. E., L. A. Frank, W. K Peterson, and W. Lennartsson, The plasma sheet boundary layer, *J Geophys. Res , 89*, 1553–1572, 1984.

Gosling, J. T., D. J. McComas, M. F. Thomsen, S J. Bame, and C. T. Russell, The warped neutral sheet and plasma sheet in the near-Earth geomagnetic tail, *J. Geophys. Res., 91*, 7093–7099, 1986.

Hirahara, M., M. Nakamura, T. Terasawa, T. Mukai, Y. Saito, T. Yamamoto, A. Nishida, S. Machida, and S. Kokubun, Acceleration and heating of cold ion beams in the plasma sheet boundary layer observed with Geotail, *Geophys. Res. Lett., 21*, 3003–3006, 1994.

Ma, C., and D. Summers, Formation of power-law energy spectra in space plasmas by stochastic acceleration due to whistler-mode waves, *Geophys. Res. Lett., 26*, 1121–1124, 1999.

Omura, Y., H. Matsumoto, T. Miyake, and H. Kojima, Electron beam instabilities as generation mechanism of electrostatic solitary waves in the magnetotail, *J. Geophys. Res., 101*, 2685–2697, 1996.

Parks, G., L. J. Chen, M. McCarthy, D. Larson, R. P. Lin, T. Phan, H. Reme, and T. Sanderson, New observations of ion beams in the plasma sheet boundary layer, *Geophys. Res Lett., 25*, 3285–3288, 1998.

Poedts, S., M. Goossens, and W. Kerner, Numerical simulation of coronal heating by resonant absorption of Alfvén waves, *Sol. Phys., 123*, 83–115, 1989.

Southwood, D. J., Some features of field line resonances in the magnetosphere, *Planet. Space Sci., 22*, 483–491, 1974.

Takahashi, K., and E. W. Hones, Jr., ISEE 1 and 2 observations of ion distributions at the plasma sheet–tail lobe boundary, *J. Geophys. Res., 93*, 8558–8582, 1988.

Tsurutani, B. T., B. E. Goldstein, and M. E. Burton, A review of the ISEE-3 geotail magnetic field results, *Planet. Space Sci., 34*, 931–960, 1986.

Verheest, F., and G. S. Lakhina, Nonresonant low-frequency instabilities in multibeam plasmas: Applications to cometary environments and plasma sheet boundary layers, *J. Geophys. Res., 96*, 7905–7910, 1991.

Walker, A. D. M., The Kelvin-Helmholtz instability in the low-latitude boundary layer, *Planet. Space Sci , 29*, 1119–1133, 1981.

Zelenyi, L , A. Galeev, and C. F. Kennel, Ion precipitation from the inner plasma sheet due to stochastic diffusion, *J. Geophys. Res., 95*, 3871–3882, 1990.

J. De Keyser, Belgian Institute for Space Aeronomy, Ringlaan 3, B-1180 Brussels, Belgium. (Johan.DeKeyser@oma.be)

(Received March 16, 1999; revised January 6, 2000; accepted January 13, 2000.)